catalysts

MDPI

Article

Dimethyl Ether Hydrolysis over WO_3/γ-Al_2O_3 Supported Catalysts

Maria Smyrnioti [1,2] and Theophilos Ioannides [1,*]

[1] Foundation for Research & Technology-Hellas, Institute of Chemical Engineering Sciences (FORTH/ICE-HT), GR-26504 Patras, Greece; msmyrnioti@iceht.forth.gr
[2] Department of Chemistry, University of Patras, GR-26504 Patras, Greece
* Correspondence: theo@iceht.forth.gr

Abstract: Dimethyl ether (DME) is considered an alternative hydrogen carrier with potential use in fuel cells and automotive and domestic applications. Dimethyl ether hydrolysis to methanol is a thermodynamically limited reaction catalyzed by solid-acid catalysts, mainly Al_2O_3 and zeolites. Moreover, it is the rate-limiting step of the DME steam reforming reaction, which is employed for the production of hydrogen fuel for fuel cell feeding. In the present study, the performance of WO_3/Al_2O_3 catalysts (0–44% wt. WO_3) was tested in DME hydrolysis reaction. The catalysts were characterized by means of N_2-physisorption, XRD, Raman spectroscopy, XPS, NH_3-TPD and 2,6-di-tert-butylpyridine adsorption experiments. The reaction rate of DME hydrolysis exhibited a volcanic trend as a function of tungsten surface density, while the best-performing catalyst was $37WO_3/Al_2O_3$, with a tungsten surface density of 7.4 W/nm^2, noting that the theoretical monolayer coverage for the specific system is 4–5 W/nm^2. Brønsted acidity was directly associated with the catalytic activity, following the same volcanic trend as a function of tungsten surface density. Blocking of Brønsted acid sites with 2,6-di-tert-butylpyridine led to a dramatic decrease in hydrolysis rates by 40 times, proving that Brønsted acid sites are primarily responsible for the catalytic activity. Thus, the type and strength rather than the concentration of acid sites are the key factors influencing the catalytic activity.

Keywords: dimethyl ether; hydrolysis; tungsten oxide; alumina; WO_3/Al_2O_3

Citation: Smyrnioti, M.; Ioannides, T. Dimethyl Ether Hydrolysis over WO_3/γ-Al_2O_3 Supported Catalysts. *Catalysts* **2022**, *12*, 396. https://doi.org/10.3390/catal12040396

Academic Editor: Leonarda Francesca Liotta

Received: 9 March 2022
Accepted: 30 March 2022
Published: 1 April 2022

1. Introduction

In recent years, the utilization of dimethyl ether (DME) as an alternative vessel for energy storage and automotive and residential applications is gaining ground. DME has been considered as an ideal candidate fuel in fuel cells due to the fact its high hydrogen-to-carbon ratio, energy density and ease in transportation and handling [1,2]. Compared to methanol, DME is non-toxic and non-corrosive. The physical properties of DME are akin to those of liquified petroleum gas (LPG); thus, the existing infrastructure can be utilized with minimal alterations for its wide distribution [3–5]. Moreover, automotive DME-fueled processors demonstrate higher overall efficiencies compared to those with gasoline, methane or ethanol [6]. It is advantageous that DME does not contain a C–C bond; therefore, it can be fully oxidized without byproducts. Additionally, DME can be used as propellant in the cosmetics industry as well as in the production of important chemicals such as dimethoxymethane (DMM), methyl acetate (MA), formaldehyde and ethylene [7–13].

DME steam reforming (SR) is regarded as the most effective way to produce high-quality reformate gas as feed for fuel cells. Reformates can be also produced by employing partial oxidation (POx) and autothermal reforming (AR) reactions [4]. DME steam reforming (Equation (1)) occurs in the temperature range 250–400 °C and involves two sequential endothermic reactions: DME hydrolysis to methanol (Equation (2)) and methanol steam reforming to hydrogen and carbon dioxide (Equation (3)).

DME Steam Reforming

$$CH_3OCH_3 + 3H_2O \rightleftharpoons 6H_2 + 2CO_2 \quad \Delta H_r^0 = +36.6 \text{ kJ mol}^{-1}, \Delta G_r^0 = +15.9 \text{ kJ mol}^{-1} \quad (1)$$

DME Hydrolysis

$$CH_3OCH_3 + H_2O \rightleftharpoons 2CH_3OH \quad \Delta H_r^0 = +35 \text{ kJ mol}^{-1}, \Delta G_r^0 = +15 \text{ kJ mol}^{-1} \quad (2)$$

Methanol Steam Reforming

$$CH_3OH + H_2O \rightleftharpoons 3H_2 + CO_2 \quad \Delta H_r^0 = +49.1 \text{ kJ mol}^{-1}, \Delta G_r^0 = -0.4 \text{ kJ mol}^{-1} \quad (3)$$

Methanol steam reforming is a well-documented reaction that takes place over Cu-, Ni-, Pt- and Pd-based catalysts [14–18]. DME hydrolysis is an equilibrium-limited, acid-catalyzed reaction and the rate-determining step of the overall DME reforming process [1]. Hence, the development of more efficient acid catalysts for DME hydrolysis in conjunction with the rapid elimination of methanol via steam reforming will contribute to the improvement of DME reforming efficiency.

Usually, the DME hydrolysis reaction is investigated along with DME steam reforming, where most of the attention is focused on the reforming catalyst, whereas the acidic one is typically Al_2O_3, being active above 250 °C [19–25]. Due to the fact of their acidic properties, zeolites have also been employed in DME hydrolysis, where they proved to be particularly active in the temperature range 150–300 °C [5,26–31]. High reaction temperatures (>300 °C) are not recommended, especially for ZSM-5 zeolites, since a methanol-to-gasoline (MTG) reaction is favored due to the fact of its high acidity [29]. Thus, care must be taken in controlling the amount, type and strength of acid sites of the employed catalysts. Other catalysts proposed as the acidic component in hybrid catalytic systems for DME steam reforming have been ZrO_2 [32], WO_3/ZrO_2 [31,33] and HPA/Al_2O_3 [34].

WO_3 is known to possess acidic properties; hence, it can be utilized in an effort to enhance the acidity of the conventional catalysts used in acid-catalyzed reactions [35,36]. Indeed, many research groups have reported on the catalytic performance of WO_x-supported catalysts over alcohol dehydration reactions [37–41]. There is a consensus that the addition of WO_x species leads to the formation of new or additional Brønsted acid sites, with suitable strength, that enhance the dehydration rate. Additionally, although they are less active than zeolites, they present very good stability, since they do not possess strong acidic sites that favor the MTG reaction and coke formation, resulting in their degradation. It has been reported that the activity of WO_x-supported catalysts over dehydration and isomerization reactions is dependent on tungsten surface density and the nature of the formed WO_x species [42]. Baertsch et al. studied the dehydration of 2-butanol over WO_x/ZrO_2 catalysts and concluded that the maximum dehydration rates were attained at intermediate tungsten surface densities, above the theoretical monolayer coverage. The improved catalytic activity was ascribed to the presence of Brønsted acid sites related to more easily reduced polytungstate species by 2-butanol. The highest reaction rates coincided with the highest density of Brønsted acid sites [43].

Due to the principle of microscopic reversibility, the catalysts employed in methanol dehydration are potential catalysts for the reverse reaction of DME hydrolysis. To the best of our knowledge, the hydrolysis of DME over WO_3/Al_2O_3-supported catalysts has not previously been reported.

In this work, WO_3/Al_2O_3-supported catalysts were synthesized via the incipient wetness impregnation method with various tungsten loadings (0–44% wt. WO_3), and they were evaluated in the DME hydrolysis reaction. The effect of tungsten surface density on the catalytic activity of the samples was investigated, and the best-performing catalyst was identified. The physicochemical characteristics of the catalysts was determined by means of N_2 physisorption, XRD, Raman spectroscopy, XPS, NH_3-TPD and 2,6-di-tert-butylpyridine adsorption experiments. Thus, the correlation between the catalytic activity and the formation of Brønsted acid sites is discussed.

2. Results

2.1. Catalyst Characterization

2.1.1. Textural and Structural Properties

The specific surface area (S_{BET}) and pore size distribution of the catalysts were determined by means of N_2 sorption measurements. N_2 adsorption–desorption isotherms and the pore size distribution of WO_3/Al_2O_3 catalysts are illustrated in Figure 1a,b, respectively. Blank γ-Al_2O_3 was also included for comparison. All isotherms could be classified as type IV with H3 hysteresis loops (IUPAC classification) closing at P/P_0 = 0.50, indicative of aggregated plate-like particles forming slit-like pores (Figure 1a). Regarding the pore size distribution estimated by the BJH method (Figure 1b), all samples were mesoporous with a mean pore diameter of 3.5–4 nm, whereas the addition of tungsten resulted in narrower pore size distribution. Table 1 summarizes the textural characteristics as well as the tungsten surface density of the supported catalysts expressed as the number of W atoms per nm^2 of catalyst. It is apparent that the specific surface area as well as the total pore volume of the catalysts systematically diminished upon augmentation of the tungsten percentage. The decrease in specific surface area was mainly caused by the diminution of the pore volume as tungsten oxo-species were formed and deposited inside the pores of the samples leading to their gradual blockage. According to the literature, the decrease in specific surface area was expected upon an increase in tungsten content [41,42,44]. Nevertheless, Said et al. reported that doping with tungsten (below 10% w/w) resulted in higher specific surface areas than the support which was attributed to the diffusion of tungsten species in Al_2O_3, leading to alterations in the textural properties of the samples [45].

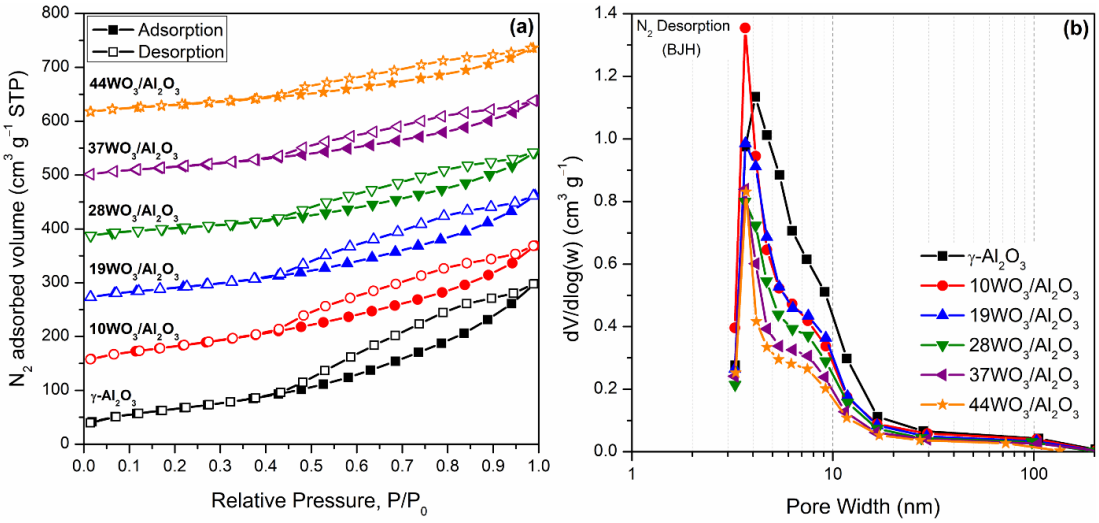

Figure 1. N_2 adsorption–desorption isotherms (**a**) and pore size distribution (**b**) of WO_3/Al_2O_3 catalysts. Isotherms in (**a**) are shifted vertically for clarity.

Table 1. Tungsten surface density, textural properties and number of acid sites, total and Brønsted, determined via NH_3-TPD and 2,6-di-tert-butylpyridine adsorption experiments, respectively.

Catalyst	W Surface Density (W/nm^2)	S_{BET} ($m^2\ g^{-1}$)	V_p ($cm^3\ g^{-1}$)	D_P (nm)	Total Acid Sites ($\mu mol\ g_{cat}^{-1}$)	Acid Sites Density ($\mu mol\ m^{-2}$)	Brønsted Acid Sites ($\mu mol\ g_{cat}^{-1}$)
γ-Al_2O_3	0.0	235	0.49	4.11	475	2.02	16
$10WO_3/Al_2O_3$	1.2	226	0.39	3.66	480	2.12	57
$19WO_3/Al_2O_3$	2.8	182	0.36	3.67	470	2.59	n.d
$28WO_3/Al_2O_3$	5.1	144	0.30	3.65	413	2.86	n.d
$37WO_3/Al_2O_3$	7.4	130	0.26	3.66	387	2.98	139
$44WO_3/Al_2O_3$	10.1	112	0.22	3.70	351	3.13	98
WO_3		2.5	0.002	3.20	n.d.	n.d.	n.d

The XRD diffractograms of WO_3/γ-Al_2O_3 catalysts are shown in Figure 2. For the supported samples up to 19% wt. WO_3/Al_2O_3, the reflections observed at 2θ = 37.3, 42.8, 45.8 and 67.1° can be ascribed exclusively to γ-Al_2O_3 support. WO_3 phases could not be detected leading to the conclusion that the tungsten species formed were either amorphous or highly dispersed on the support. Further increases in tungsten content resulted in the detection of additional reflections at 2θ = 23.5, 26.6, 28.6, 33.6, 41.4, 54.9, 60.4 and 62.4°, which could be attributed to the monoclinic WO_3 structure (JCPDS 01-083-0950, space group $P2_1/n$). WO_3 reflections became more prominent upon increment in WO_3 loading, suggesting higher crystallinity of the samples and formation of bulk WO_3. The monolayer coverage was exceeded in samples with 28% wt. WO_3 loading or higher was manifested by the detection of a crystalline WO_3 phase. According to the literature, the monolayer coverage was attained at a tungsten surface density of 4–5 W atoms/nm^2 of catalyst, which is in close agreement with our results, since the tungsten surface density of $28WO_3/Al_2O_3$ was 5.1 W/nm^2 [41,46–48].

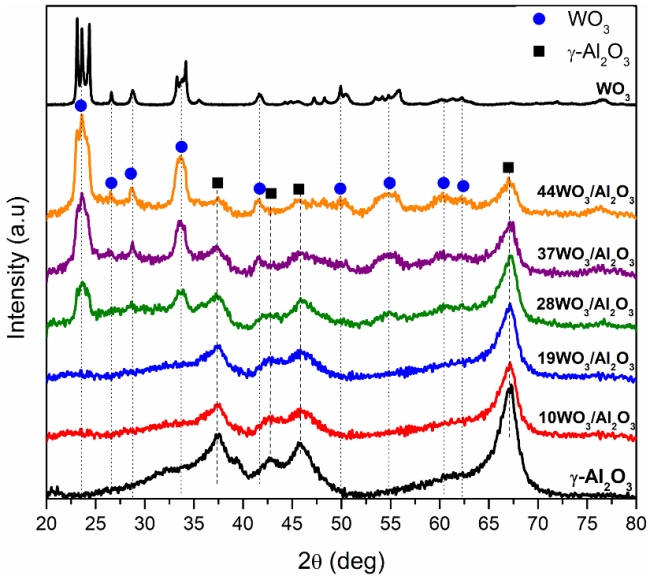

Figure 2. X-ray diffractograms of WO_3/γ-Al_2O_3 catalysts.

Raman spectra of the supported catalysts recorded under ambient conditions are presented in Figure 3. The pure WO_3 Raman spectrum w included for comparison. The only bands detected are associated with tungsten species, whereas there are no additional Raman vibrations attributed to γ-Al_2O_3. All tungsten-containing samples exhibit a characteristic band in the region 975–986 cm^{-1}, which is assigned to the symmetrical stretching mode (W = O) of tetrahedral monotungstate species. An increase in the intensity of this band was observed upon an increase in tungsten surface coverage, along with a systematic shift of its position from 975 (10% wt. WO_3) to 986 cm^{-1} (37 and 44% wt. WO_3) due to the polymerization of the amorphous monotungstates to distorted octahedral polytungstates, leading to less hydrated tungsten species on the catalyst surface [39,48]. Apart from the mono- and polytungstate species, crystalline WO_3 was also detected in the catalysts with higher tungsten loading (≥28% wt.), demonstrated by the appearance of additional bands at 275, 716 and 810 cm^{-1} attributed to the W–O–W deformation mode and W–O bending and stretching modes, respectively [49–51]. The higher the tungsten content, the sharper the bands, indicating the increase in the crystallinity of the samples. Many research groups have reported on the nature of tungsten species formed on Al_2O_3 support with the progressive increment of tungsten surface density. There is a consensus that at low surface coverage (<5 W/nm^2), tetrahedrally coordinated WO_4^{2-} species coexist with octahedrally coordinated polymeric ones, being amorphous or finely dispersed on the support. Polytungstates dominate when monolayer coverage is achieved, whereas above monolayer

coverage, WO_3 crystallites are additionally formed on top of the monolayer, in which their size increases upon further increases in the W surface density [41,49]. In the present study, the Raman results confirmed that the monolayer coverage was attained already at a 5.1 W/nm^2 surface density corresponding to $28WO_3/Al_2O_3$, since the characteristic bands of crystalline WO_3 were present. These findings are consistent with the XRD results shown in Figure 2, where bulk WO_3 was detected at tungsten surface densities equal to or higher than 5.1 W/nm^2.

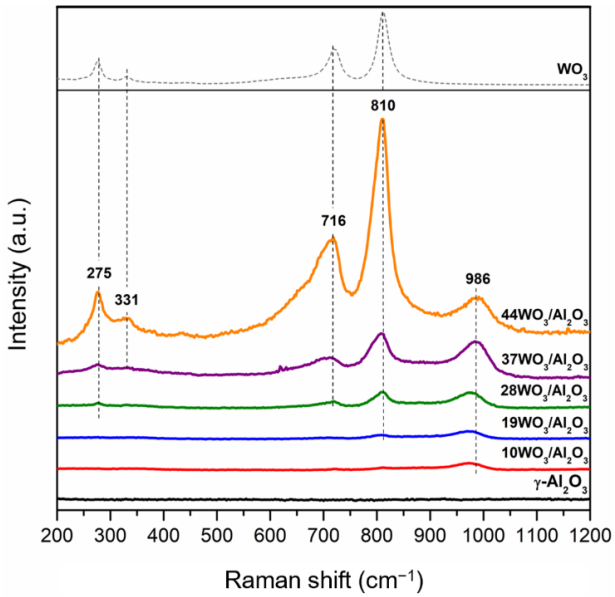

Figure 3. Raman spectra of WO_3/γ-Al_2O_3 catalysts.

2.1.2. XPS

The determination of the surface composition of the WO_3/Al_2O_3 catalysts was conducted via XPS measurements (Figure 4). According to the XP survey scan of $37WO_3/Al_2O_3$ shown in Figure 4a, the sample consists of Al, W, O and C. Similar spectra were recorded for all studied catalysts. Figure 4b presents the W4f XP spectra of 10, 19, 37 and $44WO_3/Al_2O_3$ catalysts. W4f XP spectra consist of two main peaks centered at 35.8 ± 0.1 and 37.8 ± 0.1 eV with a spin-orbit splitting of 2 eV, assigned to $W4f_{5/2}$ and $W4f_{7/2}$, respectively. These values are characteristic of the hexavalent oxidation state of tungsten (W^{6+}) and subsequent deconvolution of the spectra confirmed that W^{6+} was the only oxidation state of tungsten encountered on the examined samples [52–54]. Figure 4c exhibits the Al2p spectra of the supported catalysts. Al2p spectra comprise a main peak centered at 74.3 ± 0.1 eV, whereas no alterations were observed upon increase in tungsten content of the samples [52,53]. The O1s core level spectra of the examined catalysts consist of a main peak centered at 531 ± 0.1 eV, attributed to lattice oxygen species [55]. The binding energy values of W4f, Al2p and O1s peaks, corrected using the C1s peak at 284.5 eV, are listed in Table 2.

Table 2. Bulk and surface compositions determined via XRF and XPS measurements, respectively, expressed as the atomic ratio of W/Al and the binding energy values of W4f, Al2p and O1s peaks of WO_3/Al_2O_3 catalysts.

Catalyst	W/Al Atomic Ratio		BE (eV)			
	XRF	XPS	W4f		Al2p	O1s
			$4f_{5/2}$	$4f_{7/2}$		
$10WO_3/Al_2O_3$	0.02	0.04	37.9	35.8	74.3	531.1
$19WO_3/Al_2O_3$	0.05	0.05	37.9	35.8	74.3	531.1
$37WO_3/Al_2O_3$	0.13	0.11	37.8	35.7	74.2	530.9
$44WO_3/Al_2O_3$	0.17	0.13	37.8	35.7	74.2	531

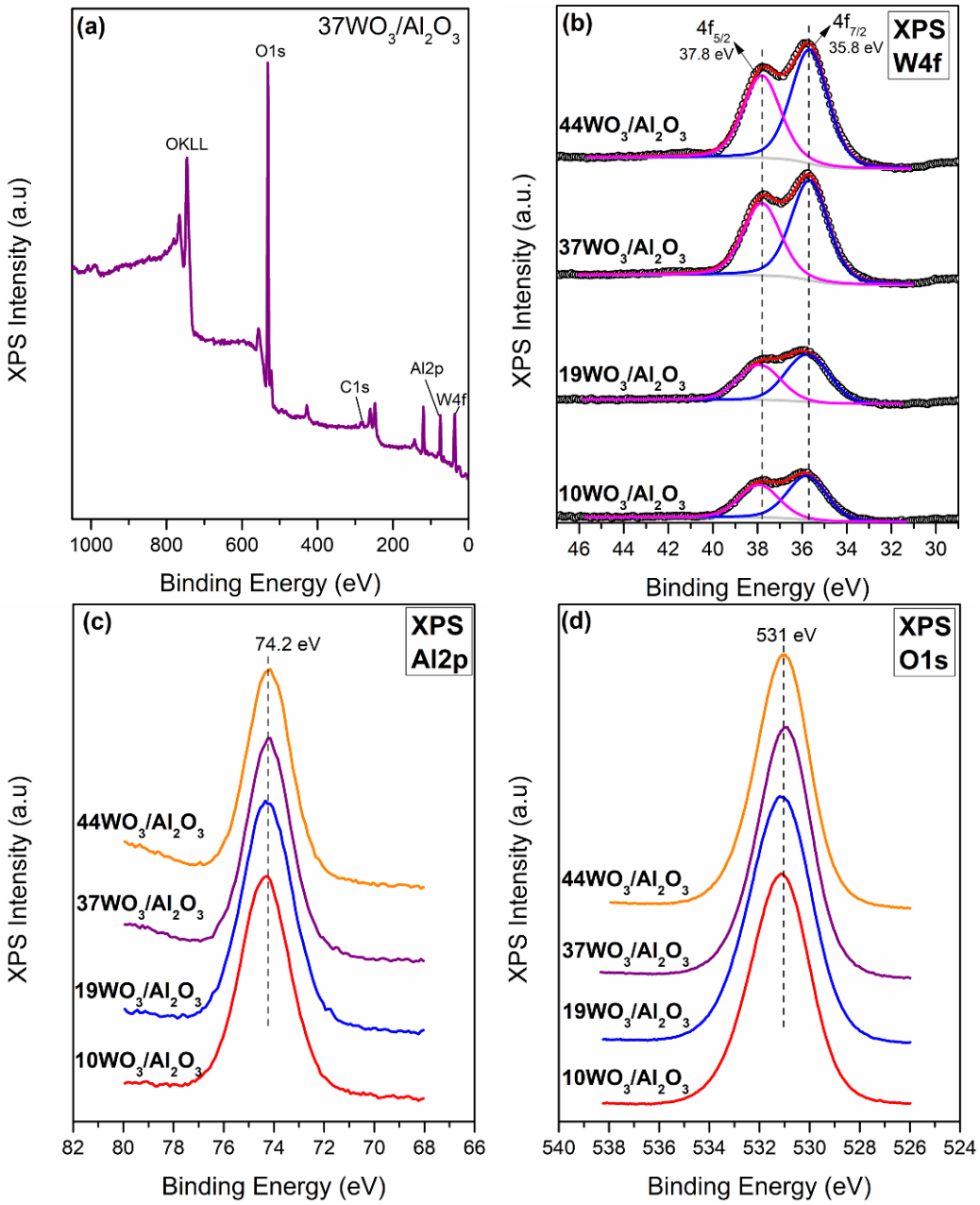

Figure 4. (**a**) Survey spectra of $37WO_3/Al_2O_3$ catalyst; (**b**) W4f XP spectra; (**c**) Al2p XP spectra; (**d**) O1s spectra of WO_3/Al_2O_3 catalysts.

The bulk and surface compositions of the catalysts determined via XRF and XPS, respectively, expressed as the atomic ratio of tungsten to aluminum (W/Al), are illustrated in Figure 5. It is apparent that at low tungsten coverage, namely, $10WO_3/Al_2O_3$, the surface W/Al atomic ratio was higher than the nominal one, i.e., the W/Al atomic ratio determined via XPS was 0.04, whereas the nominal one was 0.02. This deviation can be attributed to the high dispersion of tungsten species on the surface of the support; thus, there is a tungsten enrichment of the surface leading to a higher W/Al atomic ratio. This can also be deduced from the absence of WO_3 reflections and the characteristic bands in XRD and Raman results, respectively. Focusing on the $19WO_3/Al_2O_3$ catalyst, the bulk and surface composition were in complete agreement. For the catalysts with higher surface coverages, 37 and $44WO_3/Al_2O_3$, the surface W/Al ratios were lower than the nominal ones, and it was observed that upon increase in tungsten content, this deviation was becoming more noticeable. This can be explained by the fact that the monolayer coverage was well exceeded

on these catalysts, leading to the formation of bulk WO_3, growth of larger crystallites and, therefore, a decrease in WO_3 dispersion as tungsten loading increased. It should be noted that XPS is a surface-sensitive spectroscopic technique with an analysis depth of ~4–5 nm; hence, if larger crystallites are present on the catalyst surface, they will not be taken into account at sizes above 5 nm.

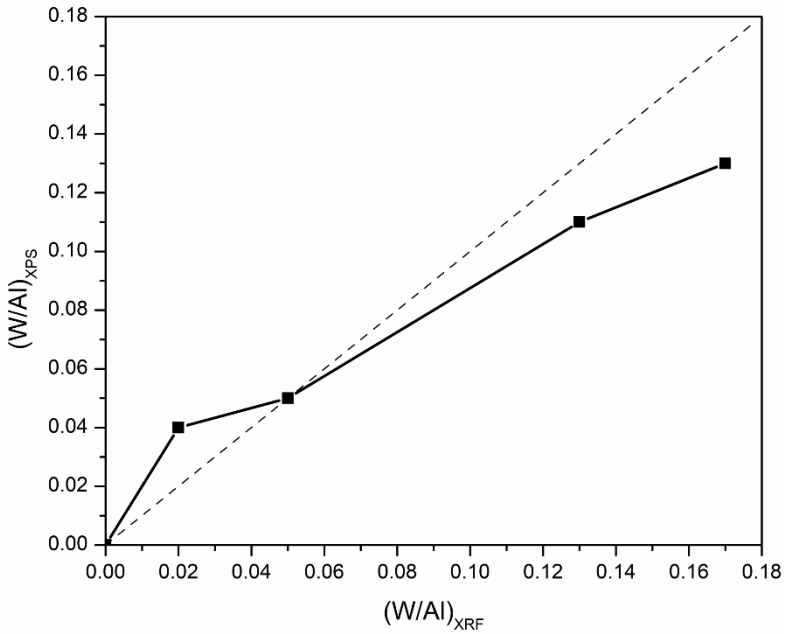

Figure 5. Surface versus bulk W/Al atomic ratios determined via XPS and XRF of WO_3/Al_2O_3 catalysts.

2.1.3. Acidity of the Catalysts

The total acidity of WO_3/Al_2O_3 catalysts was investigated by means of NH_3-TPD. The pretreated under He flow catalysts were exposed to a 1.1% NH_3/He/Ar stream up to equilibration of the adsorption process. Ar was used as an inert tracer, since it does not adsorb on the catalyst's surface. The physically adsorbed NH_3 at room temperature was flushed away by subsequent He flow through the TPD cell followed by the TPD run in the temperature region 30–650 °C. NH_3 desorbs molecularly, since it was the only species detected in the effluent. The NH_3-TPD profiles of the supported WO_3/Al_2O_3 catalysts are delineated in Figure 6a. The corresponding profile of γ-Al_2O_3 was also included for comparison. All TPD profiles consist of a main peak centered at 105–115 °C, which was extended up to 650 °C. The broad TPD profiles were indicative of the existence of both weak and intermediate acid sites on the surface of the catalysts. The addition of tungsten oxo-species did not induce any alterations regarding the strength of acid sites. The amount of NH_3 desorbed (in μmol g_{cat}^{-1}) during TPD as a function of the tungsten surface density is depicted in Figure 6b (left axis). At low surface coverages up to 2.8 W/nm^2, the amount of NH_3 desorbed and, consequently, the number of acid sites remained practically unchanged. At higher tungsten surface densities, the number of acid sites gradually decreased, which was related to the lower specific surface areas of the tungsten-containing samples. Since the catalysts significantly differed in terms of specific surface area, which plays a crucial role in the adsorption of NH_3 and, as a consequence, in the determination of the catalyst acidity, this factor can be eliminated by expressing the acidity on a surface area basis. Hence, the concentration of acid sites of the supported catalysts as a function of the tungsten surface density is demonstrated in Figure 6b (right axis). It is apparent that upon an increase in the tungsten surface coverage, a gradual increase in the density of acid sites was observed. The values of the amount and concentration of acid sites are listed in Table 1. Our results at low W surface densities are in accordance with those reported by Soled et al. [56]. They investigated the acidity of WO_3/γ-Al_2O_3 (10% wt.) employing NH_3-TPD, IR-pyridine and high-temperature gravimetric titration of amines and concluded that the addition

of tungsten at a low loading (10%) did not significantly alter the number and density of total acid sites between γ-Al_2O_3 and WO_3/Al_2O_3 catalysts but led to the formation of Brønsted at the expense of Lewis acid sites, whereas Al_2O_3 possessed only Lewis ones. The monotonic increase in Brønsted acid sites upon increase in tungsten surface density at submonolayer coverage (up to 4.1 W/nm^2) was also observed by Chen et al. [57]. They found a direct correlation between the catalytic activity in 2-propanol reaction and the evolution of Brønsted acid sites, which were mainly linked with the formation of polytungstate species over WO_x/Al_2O_3 catalysts. Zhang et al. investigated the acidity of 0–30% wt. WO_3/Al_2O_3 catalysts employing the colorimetric titration and inverse-gas chromatography techniques and concluded that in line with previous studies, Brønsted acid sites are introduced upon addition of tungsten, while the ratio of Brønsted to Lewis acid sites is systematically increasing even at high tungsten surface densities. They proposed that the cause of the Brønsted site formation is the existence of terminal oxygen atoms that lead to charge delocalization in the support [58].

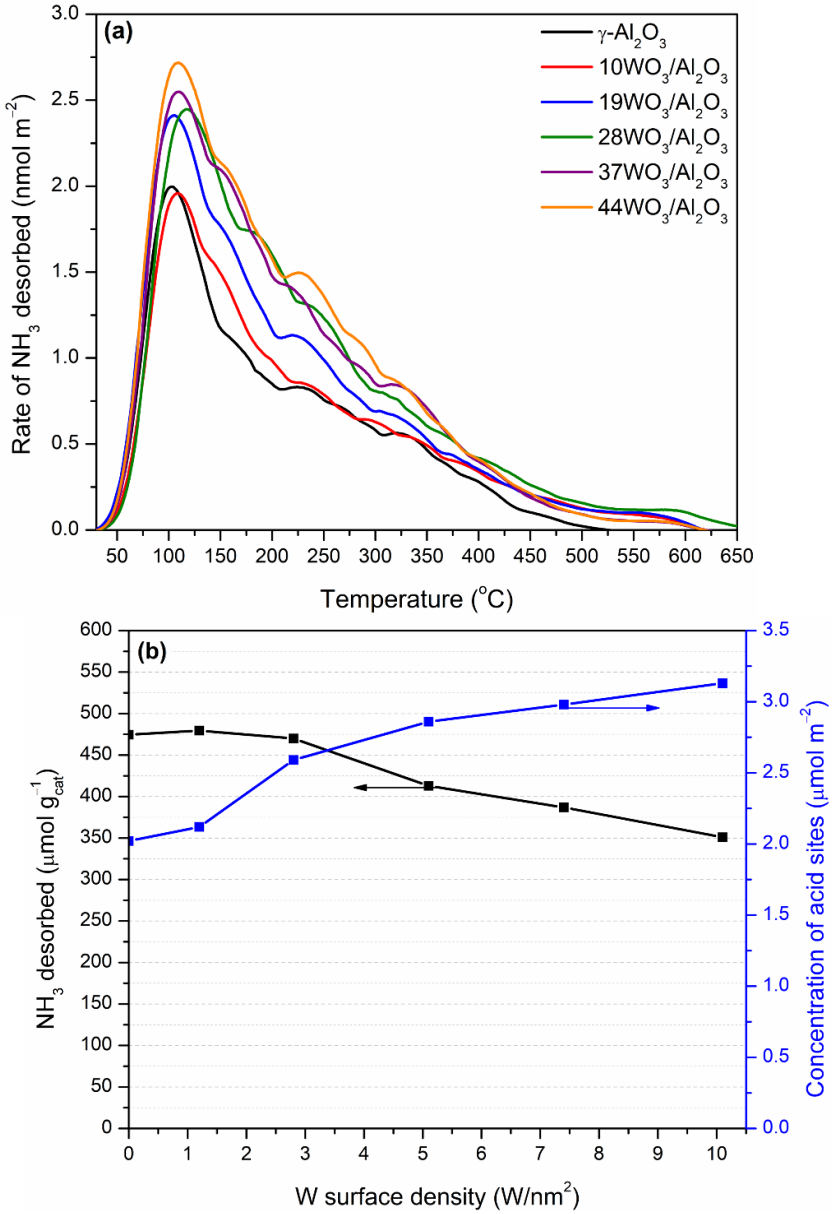

Figure 6. (**a**) NH_3-TPD profiles and (**b**) number (left axis) and concentration (right axis) of total acid sites of the WO_3/Al_2O_3 catalysts.

For the determination of Brønsted acid sites, 2,6-di-tert-butylpyridine was employed as a probe molecule. 2,6-Di-tert-butylpyridine is an alkylated pyridine with bulky tert-butyl substituents serving as hindered base that selectively adsorbs on Brønsted acid sites, forming the corresponding pyridinium ion, whereas the Lewis acid sites are inaccessible due to the steric hindrance phenomena. Many research groups have used 2,6-di-tert-butylpyridine for the discrimination between Brønsted and Lewis acid sites or the determination of Brønsted acidity on the external surface of zeolites, since the bulky substituted pyridine cannot enter into the smaller pores of the studied zeolites [37,43,59,60]. Table 1 summarizes the 2,6-di-tert-butylpyridine uptake over selected WO_3/Al_2O_3 catalysts determined via adsorption experiments at 120 °C followed by desorption of weakly adsorbed molecules at the same temperature. The uptake and consequently the amount of Brønsted acid sites follow the order $37WO_3/Al_2O_3 > 44WO_3/Al_2O_3 > 10WO_3/Al_2O_3 > Al_2O_3$. Tungsten addition results in the development of Brønsted acid sites, which increase up to 7.4 W/nm^2 in surface coverage while further increases in tungsten content lead to a decrease in Brønsted acid sites, probably linked to the formation of larger WO_3 crystallites. Macht et al. reported on the titration of Brønsted acid sites of WO_x/Al_2O_3 catalysts using 2,6-di-tert-butylpyridine during the catalytic tests in 2-butanol dehydration. They concluded that the density of Brønsted acid sites reached a maximum at above monolayer coverage (9.8 W/nm^2), whereas further increases in tungsten loading led to the diminution of the concentration of Brønsted acid sites [37]. The impact of tungsten addition on various supports on the formation of Brønsted acid sites has been reported by many research groups employing various methods [36,38,39,42,61].

2.2. Catalytic Evaluation in DME Hydrolysis

The supported WO_3/Al_2O_3 catalysts were tested in DME hydrolysis reaction in the temperature range of 140–300 °C with W/F = 0.5 g s cm^{-3}. The variation in the conversion as a function of the reaction temperature over the xWO_3/Al_2O_3 catalysts is presented in Figure 7. DME hydrolysis is a thermodynamically limited reaction; hence, the equilibrium conversion was calculated taking into account the composition of the feed, i.e., 0.09% DME and 3% H_2O vapor, and it is included in Figure 7. In the temperature range studied, CH_3OH was the only product detected. γ-Al_2O_3 is the sample with the poorest catalytic performance, where the production of CH_3OH commenced above 220 °C and reached the equilibrium value of 300 °C. Tungsten-containing catalysts demonstrated substantially improved catalytic activity. Upon increases in tungsten content, the activity of the catalysts towards DME hydrolysis gradually increased up to 37% wt. WO_3/Al_2O_3, whereas higher tungsten loading ($44WO_3/Al_2O_3$) led to inferior activity. The best-performing catalyst was already active at 150 °C and reached equilibrium at 250 °C (X_{DME} = 50%). By comparison, the temperature at which 10% conversion was achieved (T_{10}) over γ-Al_2O_3 and $37WO_3/Al_2O_3$ was 243 and 183 °C, respectively, which is a significant shift by 60 °C to lower temperatures.

Figure 8 presents the reaction rates of the WO_3/Al_2O_3 catalysts fresh and poisoned with 2,6-di-tert-butylpyridine, measured at 200 °C (left axis) and the 2,6-di-tert-butylpyridine uptake (right axis) as a function of tungsten surface density. The reaction rates are expressed on a unit mass basis, and they are measured under differential conditions ($X_{DME} \leq 20\%$). The catalytic activity in terms of reaction rates followed the order: 7.4 W/nm^2 > 10.1 W/nm^2 > 5.1 W/nm^2 > 2.8 W/nm^2 > 1.2 W/nm^2 >> γ-Al_2O_3. A direct comparison between $37WO_3/Al_2O_3$ and γ-Al_2O_3 cannot be made, since there was no measurable reaction rate at 200 °C for γ-Al_2O_3, whereas at 225 °C, where γ-Al_2O_3 exhibited catalytic activity, the conditions were not differential for the $37WO_3/Al_2O_3$ catalyst (X_{DME} = 35%). Thus, the comparison can be made by employing the sample with the lowest tungsten content, viz., $10WO_3/Al_2O_3$. Table 3 summarizes the reaction rates, the specific reaction rates and T_{10} values of the tested samples. The highest reaction rate per catalyst weight achieved by $37WO_3/Al_2O_3$ (15.74×10^{-3} μmol g_{cat}^{-1} s^{-1}) was 19 times higher than the corresponding one of $10WO_3/Al_2O_3$ (0.82×10^{-3} μmol g_{cat}^{-1} s^{-1}), while in terms of

WO_3 weight the former exhibited fivefold higher activity than $10WO_3/Al_2O_3$. Regarding the reaction rates expressed per WO_3 weight, it can be concluded that the catalytic activity increases up to 7.4 W/nm^2 where tungsten-oxo species and WO_3 crystallites (where present) developed beneficially for the hydrolysis reaction, whereas further addition of tungsten led to the formation of larger crystallites that were less active or even inert towards DME hydrolysis. The superiority of $37WO_3/Al_2O_3$ was even more pronounced in terms of intrinsic activity, which was 34 times higher than the specific reaction rate measured at 200 °C over $10WO_3/Al_2O_3$. This difference was intensified by the fact that $37WO_3/Al_2O_3$ had almost half the specific surface area of $10WO_3/Al_2O_3$, yet was significantly more active towards DME hydrolysis. At this point, it should be mentioned that the expression of the reaction rates per specific surface area was not completely appropriate for the supported catalysts, since the activity of the catalyst was mainly attributed to the supported phase and not to the entire exposed surface.

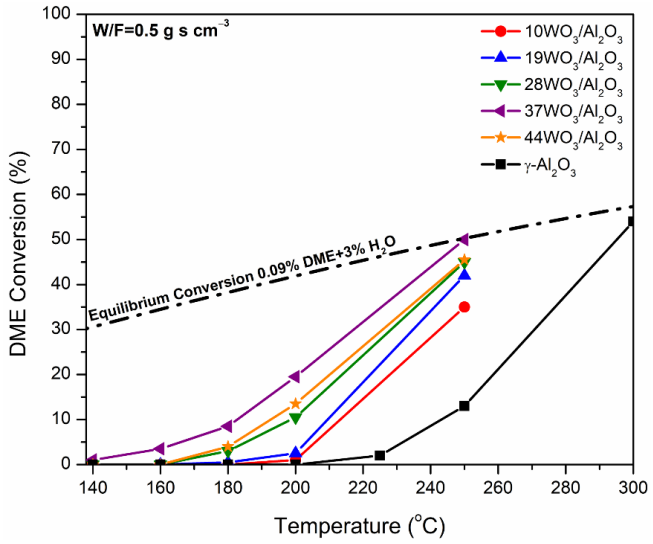

Figure 7. Conversion of DME to CH_3OH as a function of reaction temperature over WO_3/Al_2O_3 catalysts. The equilibrium conversion is also included. Reaction conditions: 0.09% DME, 3% H_2O, W/F = 0.5 g s cm^{-3}.

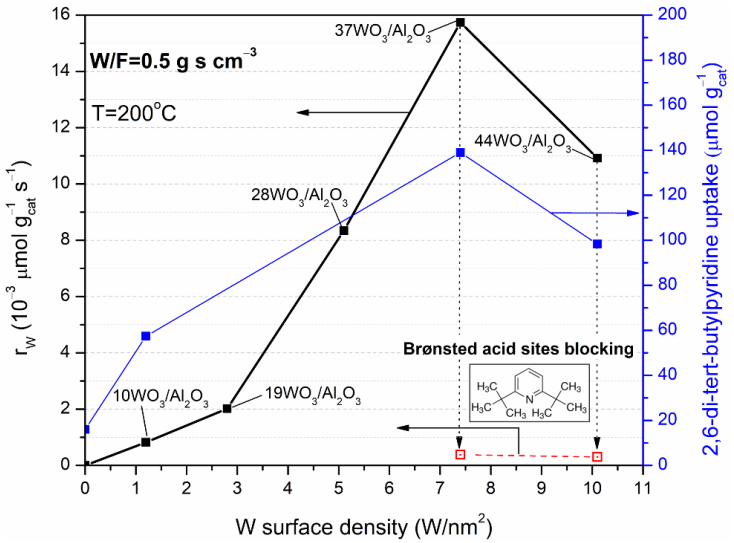

Figure 8. Variation in the reaction rates (in μmol g_{cat}^{-1} s^{-1}) of DME hydrolysis of fresh WO_3/Al_2O_3 catalysts (solid square symbols, left axis) and poisoned with 2,6-di-tert-butylpyridine prior to catalytic tests (open square symbols, left axis) and 2,6-di-ter-butylpyridine uptake (right axis) with the tungsten surface density. Reaction conditions: 0.09% DME, 3% H_2O, reaction temperature = 200 °C, W/F = 0.5 g s cm^{-3}.

Table 3. Catalytic performance of WO_3/Al_2O_3 in DME hydrolysis expressed as the temperature at which 10% conversion was obtained (T_{10}) and reaction rates expressed per catalyst weight, WO_3 weight and specific surface area, r_W, r_{WO_3} and r, respectively.

Catalyst	T_{10} (°C)	r_W ($\times 10^{-3}$ μmol g_{cat}^{-1} s^{-1})	r_{WO_3} ($\times 10^{-3}$ μmol g_{WO3}^{-1} s^{-1})	r ($\times 10^{-5}$ μmol m^{-2} s^{-1})
γ-Al_2O_3	243	0	n.d.	0
$10WO_3/Al_2O_3$	213	0.82	8.2	0.36
$19WO_3/Al_2O_3$	210	2.02	10.64	1.11
$28WO_3/Al_2O_3$	199	8.34	29.78	5.77
$37WO_3/Al_2O_3$	192	15.74	42.54	12.11
$44WO_3/Al_2O_3$	183	10.92	25.10	9.73

In any case, the activity of the supported WO_3/Al_2O_3 catalysts exhibited a volcanic trend in DME hydrolysis, and the best-performing catalyst was the one with 7.4 W/nm^2. The same trend was found for the 2,6-di-tert-butlypyridine uptake as shown in Figure 8 (right axis). As previously discussed (Section 2.1.3), 2,6-di-tert-butylpyridine uptake was directly associated with the number of Brønsted acid sites formed on the surface of the catalysts; thus, it can be concluded that DME hydrolysis occurred primarily on the Brønsted acid sites of WO_3/Al_2O_3 catalysts. To further confirm the role of Brønsted acid sites on the catalytic activity of the tungsten-containing catalysts, DME hydrolysis rates were also measured after blocking the Brønsted acid sites of the best-performing samples, namely, $37WO_3/Al_2O_3$ and $44WO_3/Al_2O_3$, with 2,6-di-tert-butylpyridine (Figure 8, left axis). Prior to catalytic tests at 200 °C, 2,6-di-tert-butylpyridine was adsorbed on the samples at 120 °C overnight followed by the desorption of weakly bound molecules at the same temperature. Indeed, the reaction rates obtained over poisoned $37WO_3/Al_2O_3$ and $44WO_3/Al_2O_3$ were 0.39×10^{-3} and 0.30×10^{-3} μmol g_{cat}^{-1} s^{-1} compared to 15.74×10^{-3} and 10.92×10^{-3} μmol g_{cat}^{-1} s^{-1} of the fresh samples. Therefore, even though the reaction took place at 200 °C, Brønsted acid sites were blocked by a part of 2,6-di-tert-butylpyridine that remained strongly chemisorbed on them, resulting in a dramatic decrease in the reaction rates by 36–40 times. Thus, it can be concluded that DME hydrolysis primarily occurs on Brønsted acid sites, whereas the residual reaction rates measured may be attributed to Lewis acid sites on WO_x domains that remained unaffected by the addition of 2,6-di-tert-butylpyridine [37].

Since there are no reports in DME hydrolysis over supported WO_x catalysts and because of the principle of microscopic reversibility, we took into consideration the literature concerning alcohol dehydration reactions. Suwannapichat et al. investigated the direct synthesis of DME from CO_2 hydrogenation over hybrid $CuO/ZnO/ZrO_2$ and WO_x/Al_2O_3 catalysts. Methanol dehydration took place over tungsten-supported catalysts varying the tungsten loading and the pore size of the support. In accordance with our results, they also observed a volcanic trend in DME production as a function of tungsten surface density, while the maximum value was obtained above monolayer coverage at 8 W/nm^2 [41]. The optimization of the catalytic activity in alcohol dehydration above the theoretical monolayer coverage over WO_x-supported catalysts (i.e., WO_x/ZrO_2 and WO_x/TiO_2) was reported by various research groups [37,39,40,62]. It is widely accepted that CH_3OH dehydration as well as the reverse reaction, DME hydrolysis, are acid-catalyzed reactions; hence, the acidity of the catalysts plays a crucial role in the overall process. However, based on the NH_3-TPD results (Figure 6b), it can be seen that the most active catalysts in DME hydrolysis exhibited lower total acidity (per catalyst weight). Adsorption of NH_3 is a measure of the total acidity of the catalysts, both Brønsted and Lewis; thus, no direct correlation could be made between the total acidity and the catalytic activity. Therefore, the type and strength rather than the number of the acid sites are the key factors that drive the catalytic activity. Indeed, it is generally agreed that mainly Brønsted acid sites are responsible for the higher reaction rates obtained in DME hydrolysis and CH_3OH dehydration [5,39,63–66]. γ-Al_2O_3 that possesses only Lewis acid sites has low activity, as water competitively adsorbs on the same sites with methanol leading to their blockage [64,67]. Macht et al. concluded that the

enhanced catalytic activity in 2-butanol dehydration over WO_3/Al_2O_3 and WO_3/ZrO_2 is directly correlated with the development Brønsted acidity. Lewis acid sites were constantly diminishing upon tungsten addition on Al_2O_3. The dehydration rates increased upon tungsten surface density increment, reaching the maximum values at 9–10 W/nm^2. After the titration of the Brønsted acid sites with 2,6-di-tert-butylpyridine, the dehydration rates obtained dramatically decreased. The residual reaction rates remained constant upon increase in tungsten surface density up to 10 W/nm^2, while at even higher surface densities, where large WO_3 crystallites were formed, they diminished further. On the other hand, the blocking of acid sites with pyridine, which coordinated with both Brønsted and Lewis acid sites, led to the complete loss of the dehydration activity of the catalysts [37]. The results obtained in the present work regarding the enhanced catalytic activity of the WO_3/Al_2O_3 catalysts in DME hydrolysis could, therefore, be directly associated with the development of Brønsted acid sites upon tungsten addition on Al_2O_3 support. A DME molecule adsorbs on a Brønsted acid site forming a dimethyloxonium ion ($(CH_3)_2OH^+$), whereas its subsequent hydration leads to the formation of methanol.

3. Materials and Methods

3.1. Catalysts Synthesis

WO_3/γ-Al_2O_3 samples with tungsten (VI) oxide loading in the range 0–44% *w*/*w* were prepared via the incipient wetness impregnation method. Prior to impregnation, the γ-Al_2O_3 (ALCOA DD-2) support was crushed, sieved ($90 < d_p < 180$ μm) and calcined at 500 °C for 4 h at a heating rate of 5 °C min^{-1}. The desired amount of ammonium metatungstate hydrate ($(NH_4)_6W_{12}O_{39}{\cdot}xH_2O$, Sigma Aldrich, Steinheim, Germany), depending on the final percentage of WO_3 on the catalyst, was dissolved in triple-distilled water followed by the impregnation of the support. The suspension was left for equilibration under rotation for 1 h at room temperature and atmospheric pressure, while subsequent evaporation under vacuum at 50 °C led to a slurry which was left to dry at room temperature overnight. The samples were further dried by gradually increasing the temperature from 50 to 120 °C with a heating rate of 10 °C h^{-1} and, finally, they were calcined at 500 °C with a heating rate of 5 °C min^{-1} for 5 h. The resulting catalysts were nominated as xWO_3/Al_2O_3 (where x refers to the WO_3 loading by weight percent, i.e., 0, 10, 19, 28, 37, and 44%).

3.2. Catalyst Characterization

The specific surface area (S_{BET}) and porosity of the catalysts were determined from the N_2 sorption-isotherms at −196 °C, using a Quantachrome Autosorb IQ-C-MP apparatus. Prior to measurements, the samples were degassed at 150 °C in vacuum for 2 h. N_2 adsorption isotherms were measured at relative pressures (P/P_0, where P is the actual pressure of N_2, and P_0 is the saturation pressure of N_2 at −196 °C) in the range of 0.015 to 0.995. The specific surface area was calculated in the range $0.015 < P/P_0 < 0.35$, total pore volume at $P/P_0 = 0.995$ and pore size distribution (PSD) using the Barret–Joyner–Halenda (BJH) model using the desorption branches of the N_2 isotherms.

The XRD diffractograms of the catalysts were recorded using a Bruker D8 Advance X-ray powder diffractometer operated at 40 mA and 40 kV employing a Ni-filtered Cu Ka radiation (λ = 1.5418 Å) in the range of $20° < 2\theta < 80°$ with a scan step of 0.02° and a scan speed of 1.5 s/step.

Raman spectra were recorded using a T64000 micro-Raman spectrometer (Horiba Jobin Yvon, Kyoto, Japan) equipped with a 514.5 nm laser line as the excitation source. The spot size was ~2–3 μm while a microscope objective of 50× magnification was employed. The spectra were corrected taking into account the 520 cm^{-1} Raman band of crystalline Si.

The composition of the catalysts was determined via X-ray fluorescence spectroscopy (XRF) using a S2 PicofoxTM Bruker Nano X-Ray Fluorescence spectrometer equipped with a metal–ceramic air-cooled molybdenum (Mo) target X-ray tube operating at 50 kV and 0.6 mA.

X-ray photoelectron spectroscopy (XPS) was performed in a UHV chamber (5×10^{-10} mbar) equipped with a SPECS Phoibos 100-1D-DLD hemispherical electron analyzer and a non-monochromatized dual-anode Mg/Al X-ray source. Samples were excited using MgKα at 1253.6 eV photon energy, and the pass energy of the analyzer was 10 eV. Prior to XPS measurements, the powdered samples were pressed and pelletized, whereas the diameter of the analyzed area spot was 7×15 mm. The spectra were recorded and analyzed using the commercial software, SpecsLab Prodigy (Specs GmbH, Berlin, Germany). The binding energy at 284.5 eV corresponding to C 1s of contaminant carbon was used as reference for the calculation of the binding energies.

The total acidity of the catalysts was determined via temperature-programmed desorption of ammonia (NH_3-TPD) under atmospheric pressure in a fixed-bed reactor. The system consisted of two independent gas lines equipped with mass flow controllers (Aera GmbH, Kirchheim, Germany) and a mass spectrometer (Omnistar/Pfeiffer Vacuum, Asslar, Germany) for online monitoring of effluent gases. During NH_3 adsorption at room temperature, a gas mixture (30 cm^3 min^{-1}) containing 1.1% NH_3, 1% Ar as inert tracer and He as balance was fed into the TPD cell (100 mg of catalyst) until saturation was attained, marked by the stabilization of signals in the mass spectrometer. Then, the excess of NH_3 was purged with He until all signals met their baselines. The subsequent TPD run was conducted under He flow (30 cm^3 min^{-1}) from 30 to 650 °C with a heating rate of 10 °C min^{-1}. Prior to NH_3 adsorption, the samples were preheated under He flow (30 cm^3 min^{-1}) up to 500 °C with a heating rate of 10 °C min^{-1} and soaked at 500 °C for 15 min followed by cooling down to room temperature under the same flow. The following fragments were recorded in the mass spectrometer during TPD experiments: m/z = 15, 16 (CH_4), 17 (NH_3), 18 (H_2O), 28 (N_2), 44 (CO_2), 32 (O_2), 40 (Ar) and 2 (H_2).

The 2,6-di-tert-butylpyridine (>98%, Merck-Schuchardt, Hohenbrunn, Germany) was used as probe molecule for the determination of Brønsted acid sites of WO_3/Al_2O_3 catalysts via a static gravimetric method. In brief, vapors of 2,6-di-tert-butylpyridine were left to adsorb on the powdered samples (dried at 150 °C overnight) enclosed in a sealed glass vessel at 120 °C overnight with a subsequent desorption at the same temperature to remove the weakly bound 2,6-di-tert-butylpyridine. After the adsorption and desorption process, the weight gain and loss, respectively, were measured. The 2,6-di-tert-butylpyridine uptake is referred to the remaining adsorbed amount of 2,6-di-tert-butylpyridine after the desorption step.

3.3. Catalyst Evaluation Tests

The catalytic performance of WO_3/γ-Al_2O_3 samples in DME hydrolysis was carried out in a conventional quartz fixed-bed flow reactor at atmospheric pressure whereas the reaction temperature was in the range of 140–300 °C. In a typical experiment, 0.5 g of catalyst (crushed and sieved to particle size $90 < dp < 180$ μm) was introduced in the reactor and heated under He (30 cm^3 min^{-1}) at 300 °C for 1 h. Then, the catalyst was exposed to a reactant feed (60 cm^3 min^{-1}) containing 900 ppm DME (3.5% DME/He, home-made mixture in gas cylinder using DME, ≥99.9% (GC), Sigma Aldrich, Steinheim, Germany), ~3% H_2O and He (99.999%, Linde Hellas, Athens, Greece) as balance (W/F = 0.5 g s cm^{-3}). H_2O vapor was introduced by flowing He through a saturator containing triple-distilled water at room temperature. The reactant and product composition were analyzed online by a gas chromatograph (Shimadzu GC-14B) equipped with a flame ionization detector (FID). The employed chromatographic column was 0.19% Picric acid/Graphpac-CC 80/100, $7' \times 1/8'' \times 0.085''$/SS.

The measurements of the reaction rates over the poisoned catalysts with 2,6-di-tert-butylpyridine took place at 200 °C with no alterations regarding the reactant feed or the W/F. Prior to the experiment, the sample was exposed to 2,6-di-tert-butylpyridine vapors in a sealed vessel at 120 °C overnight followed by the removal of excess 2,6-di-tert-butylpyridine at the same temperature. Then, the catalyst was loaded in the reactor, and

the feed stream passed though the reactor at 200 °C. The reaction rate was measured after steady state was achieved (~1 h).

The conversion (X) of DME was calculated using the following equation:

$$X_{DME}(\%) = \frac{C^{in}_{DME} - C^{out}_{DME}}{C^{in}_{DME}} \times 100 = \frac{\frac{C^{out}_{CH_3OH}}{2}}{C^{in}_{DME}} \times 100 \quad (4)$$

where C^{in}_{DME}, C^{out}_{DME} and $C^{out}_{CH_3OH}$ are the feed and the outlet concentration of DME and CH_3OH, respectively.

For the calculation of the reaction rates on a unit catalyst weight (r_W, in μmol $g_{cat}{}^{-1}$ s^{-1}) the following equation was used:

$$r_W = \frac{F_{DME}\, X_{DME}}{W} \quad (5)$$

where: F_{DME} is the molar flow of DME (in μmol s^{-1}), X_{DME} is the conversion of DME to CH_3OH and W is the catalyst weight (in g).

For the calculation of the reaction rates per WO_3 weight (r_{WO_3}, in μmol $g_{WO3}{}^{-1}$ s^{-1}) the following equation was used:

$$r_{WO_3} = \frac{r_W}{w} \quad (6)$$

where r_W is the reaction rate on a unit catalyst weight of DME hydrolysis (in μmol $g_{cat}{}^{-1}$ s^{-1}), and w is the WO_3 weight calculated from the WO_3 content of the catalyst (in g).

For the calculation of the specific reaction rates (r, in μmol m^{-2} s^{-1}), the following equation was used:

$$r = \frac{r_W}{SSA} \quad (7)$$

where r_W is the reaction rate on a unit catalyst weight of DME hydrolysis (in μmol $g_{cat}{}^{-1}$ s^{-1}), and SSA is the specific surface area of the catalysts (in m^2 $g_{cat}{}^{-1}$).

4. Conclusions

DME hydrolysis is the rate-determining step in steam reforming of DME, which can be employed in the production of high-quality reformate gas as feed for fuel cells. Hence, the improvement of DME hydrolysis reaction would lead to the enhanced efficiency of the overall DME steam reforming process. Acidic Al_2O_3 and zeolites were mainly used to catalyze the reaction, with the former being inactive beyond 250 °C and the latter being active but not stable due to the coke formation resulting from the simultaneous occurrence of side reactions such as an MTG reaction. Therefore, the modification of γ-Al_2O_3 focusing on the development of additional acid sites would lead to enhanced catalytic activity at a lower temperature and, at the same time, its high stability could be retained. WO_3/Al_2O_3-supported catalysts with various WO_3 loadings (0–44% wt.), prepared by the incipient wetness impregnation method, were investigated in DME hydrolysis to CH_3OH. According to XRD and Raman results, amorphous and well-dispersed mono- and polytungstate species prevailed on the surface of the catalysts at low tungsten surface densities (<5.1 W/nm^2), whereas monolayer coverage was exceeded at higher surface densities (≥5.1 W/nm^2) indicated by the formation of WO_3 crystallites. XPS measurements further validated the fine dispersion of tungsten oxo-species at low surface coverage, whereas W^{6+} was the only oxidation state encountered on the samples. The concentration of acid sites determined via NH_3-TPD experiments as a function of tungsten loading exhibited a monotonic increase, although the amount of total acid sites per catalyst unit weight decreased due to the specific surface area loss of the samples upon augmentation of tungsten content. A volcanic trend was observed between the hydrolysis rates and the tungsten surface density. The number of Brønsted acid sites, determined via the selective adsorption of 2,6-di-tert-butylpyridine as a function of tungsten surface density, followed the same trend.

The most active catalyst was $37WO_3/Al_2O_3$ with a tungsten surface density of 7.4 W/nm^2, which is above the theoretical monolayer coverage. Blocking of Brønsted acid sites with 2,6-di-tert-butylpyridine led to a dramatic decrease in hydrolysis rates by 40 times. The enhanced catalytic activity was attributed to the development of Brønsted acid sites at the expense of Lewis ones upon tungsten addition. Therefore, the type and strength rather than the number of acid sites have a key role in DME hydrolysis reaction.

Author Contributions: M.S., Methodology, validation, formal analysis, investigation, data curation, and writing—original draft preparation; T.I., Conceptualization, methodology, validation, formal analysis, investigation, resources, writing—review and editing, supervision, project administration, and funding acquisition. All authors have read and agreed to the published version of the manuscript.

Funding: This research was co-financed by the European Union and Greek national funds through the Operational Program Competitiveness, Entrepreneurship and Innovation under the call RESEARCH–CREATE–INNOVATE (project code: T1EDK-01704).

Data Availability Statement: The data presented in this study are available on request from the corresponding author.

Acknowledgments: The authors would like to thank L. Sygellou for her assistance with the XPS measurements and Paraskevopoulou for the donation of the 2,6-di-tert-butylpyridine reagent.

Conflicts of Interest: The authors declare no conflict of interest.

References

1. Namuangruk, S.; Meeprasert, J.; Khemthong, P.; Faungnawakij, K. A Combined Experimental and Theoretical Study on the Hydrolysis of Dimethyl Ether over H-ZSM-5. *J. Phys. Chem. C* **2011**, *115*, 11649–11656. [CrossRef]
2. Hirunsit, P.; Faungnawakij, K.; Namuangruk, S.; Luadthong, C. Catalytic Behavior and Surface Species Investigation over γ-Al_2O_3 in Dimethyl Ether Hydrolysis. *Appl. Catal. Gen.* **2013**, *460–461*, 99–105. [CrossRef]
3. Olah, G.A.; Goeppert, A.; Prakash, G.K.S. Chemical Recycling of Carbon Dioxide to Methanol and Dimethyl Ether: From Greenhouse Gas to Renewable, Environmentally Carbon Neutral Fuels and Synthetic Hydrocarbons. *J. Org. Chem.* **2009**, *74*, 487–498. [CrossRef] [PubMed]
4. Faungnawakij, K.; Kikuchi, R.; Matsui, T.; Fukunaga, T.; Eguchi, K. A Comparative Study of Solid Acids in Hydrolysis and Steam Reforming of Dimethyl Ether. *Appl. Catal. Gen.* **2007**, *333*, 114–121. [CrossRef]
5. Semelsberger, T.A.; Ott, K.C.; Borup, R.L.; Greene, H.L. Role of Acidity on the Hydrolysis of Dimethyl Ether (DME) to Methanol. *Appl. Catal. B Environ.* **2005**, *61*, 281–287. [CrossRef]
6. Semelsberger, T.A.; Borup, R.L.; Greene, H.L. Dimethyl Ether (DME) as an Alternative Fuel. *J. Power Sources* **2006**, *156*, 497–511. [CrossRef]
7. Fleisch, T.H.; Basu, A.; Gradassi, M.J.; Masin, J.G. Dimethyl Ether: A Fuel for the 21st Century. In *Studies in Surface Science and Catalysis*; Elsevier: Amsterdam, The Netherlands, 1997; Volume 107, pp. 117–125. ISBN 978-0-444-82352-6.
8. Liu, H.; Iglesia, E. Selective One-Step Synthesis of Dimethoxymethane via Methanol or Dimethyl Ether Oxidation on $H_{3+n}V_nMo_{12-n}PO_{40}$ Keggin Structures. *J. Phys. Chem. B* **2003**, *107*, 10840–10847. [CrossRef]
9. Zhang, Q.; Tan, Y.; Yang, C.; Han, Y. $MnCl_2$ Modified $H_4SiW_{12}O_{40}/SiO_2$ Catalysts for Catalytic Oxidation of Dimethy Ether to Dimethoxymethane. *J. Mol. Catal. Chem.* **2007**, *263*, 149–155. [CrossRef]
10. Cheung, P.; Bhan, A.; Sunley, G.; Law, D.; Iglesia, E. Site Requirements and Elementary Steps in Dimethyl Ether Carbonylation Catalyzed by Acidic Zeolites. *J. Catal.* **2007**, *245*, 110–123. [CrossRef]
11. Zhou, W.; Kang, J.; Cheng, K.; He, S.; Shi, J.; Zhou, C.; Zhang, Q.; Chen, J.; Peng, L.; Chen, M.; et al. Direct Conversion of Syngas into Methyl Acetate, Ethanol, and Ethylene by Relay Catalysis via the Intermediate Dimethyl Ether. *Angew. Chem. Int. Ed.* **2018**, *57*, 12012–12016. [CrossRef]
12. Liu, H.; Cheung, P.; Iglesia, E. Zirconia-Supported MoO_xCatalysts for the Selective Oxidation of Dimethyl Ether to Formaldehyde: Structure, Redox Properties, and Reaction Pathways. *J. Phys. Chem. B* **2003**, *107*, 4118–4127. [CrossRef]
13. Peláez, R.; Marín, P.; Ordóñez, S. Synthesis of Formaldehyde from Dimethyl Ether on Alumina-Supported Molybdenum Oxide Catalyst. *Appl. Catal. Gen.* **2016**, *527*, 137–145. [CrossRef]
14. Palo, D.R.; Dagle, R.A.; Holladay, J.D. Methanol Steam Reforming for Hydrogen Production. *Chem. Rev.* **2007**, *107*, 3992–4021. [CrossRef] [PubMed]
15. Sá, S.; Silva, H.; Brandão, L.; Sousa, J.M.; Mendes, A. Catalysts for Methanol Steam Reforming—A Review. *Appl. Catal. B Environ.* **2010**, *99*, 43–57. [CrossRef]
16. Papavasiliou, J.; Avgouropoulos, G.; Ioannides, T. Steam Reforming of Methanol over Copper–Manganese Spinel Oxide Catalysts. *Catal. Commun.* **2005**, *6*, 497–501. [CrossRef]

17. Liu, Y.; Hayakawa, T.; Suzuki, K.; Hamakawa, S.; Tsunoda, T.; Ishii, T.; Kumagai, M. Highly Active Copper/Ceria Catalysts for Steam Reforming of Methanol. *Appl. Catal. Gen.* **2002**, *223*, 137–145. [CrossRef]
18. Ranganathan, E.S.; Bej, S.K.; Thompson, L.T. Methanol Steam Reforming over Pd/ZnO and Pd/CeO_2 Catalysts. *Appl. Catal. Gen.* **2005**, *289*, 153–162. [CrossRef]
19. Tanaka, Y.; Kikuchi, R.; Takeguchi, T.; Eguchi, K. Steam Reforming of Dimethyl Ether over Composite Catalysts of γ-Al_2O_3 and Cu-Based Spinel. *Appl. Catal. B Environ.* **2005**, *57*, 211–222. [CrossRef]
20. Faungnawakij, K.; Tanaka, Y.; Shimoda, N.; Fukunaga, T.; Kikuchi, R.; Eguchi, K. Hydrogen Production from Dimethyl Ether Steam Reforming over Composite Catalysts of Copper Ferrite Spinel and Alumina. *Appl. Catal. B Environ.* **2007**, *74*, 144–151. [CrossRef]
21. Faungnawakij, K.; Shimoda, N.; Fukunaga, T.; Kikuchi, R.; Eguchi, K. Cu-Based Spinel Catalysts CuB_2O_4 (B=Fe, Mn, Cr, Ga, Al, $Fe_{0.75}Mn_{0.25}$) for Steam Reforming of Dimethyl Ether. *Appl. Catal. Gen.* **2008**, *341*, 139–145. [CrossRef]
22. Faungnawakij, K.; Shimoda, N.; Fukunaga, T.; Kikuchi, R.; Eguchi, K. Crystal Structure and Surface Species of $CuFe_2O_4$ Spinel Catalysts in Steam Reforming of Dimethyl Ether. *Appl. Catal. B Environ.* **2009**, *92*, 341–350. [CrossRef]
23. Wang, X.; Pan, X.; Lin, R.; Kou, S.; Zou, W.; Ma, J.-X. Steam Reforming of Dimethyl Ether over Cu–Ni/γ-Al_2O_3 Bi-Functional Catalyst Prepared by Deposition–Precipitation Method. *Int. J. Hydrogen Energy* **2010**, *35*, 4060–4068. [CrossRef]
24. Takeishi, K.; Akaike, Y. Hydrogen Production by Dimethyl Ether Steam Reforming over Copper Alumina Catalysts Prepared Using the Sol–Gel Method. *Appl. Catal. Gen.* **2016**, *510*, 20–26. [CrossRef]
25. Shimoda, N.; Faungnawakij, K.; Kikuchi, R.; Fukunaga, T.; Eguchi, K. Catalytic Performance Enhancement by Heat Treatment of $CuFe_2O_4$ Spinel and γ-Alumina Composite Catalysts for Steam Reforming of Dimethyl Ether. *Appl. Catal. Gen.* **2009**, *365*, 71–78. [CrossRef]
26. Kawabata, T.; Matsuoka, H.; Shishido, T.; Li, D.; Tian, Y.; Sano, T.; Takehira, K. Steam Reforming of Dimethyl Ether over ZSM-5 Coupled with Cu/ZnO/Al_2O_3 Catalyst Prepared by Homogeneous Precipitation. *Appl. Catal. Gen.* **2006**, *308*, 82–90. [CrossRef]
27. Shimoda, N.; Faungnawakij, K.; Kikuchi, R.; Eguchi, K. A Study of Various Zeolites and $CuFe_2O_4$ Spinel Composite Catalysts in Steam Reforming and Hydrolysis of Dimethyl Ether. *Int. J. Hydrogen Energy* **2011**, *36*, 1433–1441. [CrossRef]
28. Ereña, J.; Vicente, J.; Aguayo, A.T.; Gayubo, A.G.; Olazar, M.; Bilbao, J. Effect of Combining Metallic and Acid Functions in CZA/HZSM-5 Desilicated Zeolite Catalysts on the DME Steam Reforming in a Fluidized Bed. *Int. J. Hydrogen Energy* **2013**, *38*, 10019–10028. [CrossRef]
29. Feng, D.; Zuo, Y.; Wang, D.; Wang, J. Steam Reforming of Dimethyl Ether over Coupled Catalysts of CuO-ZnO-Al_2O_3-ZrO_2 and Solid-Acid Catalyst. *Chin. J. Chem. Eng.* **2009**, *17*, 64–71. [CrossRef]
30. Fukunaga, T.; Ryumon, N.; Shimazu, S. The Influence of Metals and Acidic Oxide Species on the Steam Reforming of Dimethyl Ether (DME). *Appl. Catal. Gen.* **2008**, *348*, 193–200. [CrossRef]
31. Matsumoto, T.; Nishiguchi, T.; Kanai, H.; Utani, K.; Matsumura, Y.; Imamura, S. Steam Reforming of Dimethyl Ether over H-Mordenite-Cu/CeO_2 Catalysts. *Appl. Catal. Gen.* **2004**, *276*, 267–273. [CrossRef]
32. Semelsberger, T.A.; Ott, K.C.; Borup, R.L.; Greene, H.L. Generating Hydrogen-Rich Fuel-Cell Feeds from Dimethyl Ether (DME) Using Cu/Zn Supported on Various Solid-Acid Substrates. *Appl. Catal. Gen.* **2006**, *309*, 210–223. [CrossRef]
33. Nishiguchi, T.; Oka, K.; Matsumoto, T.; Kanai, H.; Utani, K.; Imamura, S. Durability of WO_3/ZrO_2–CuO/CeO_2 Catalysts for Steam Reforming of Dimethyl Ether. *Appl. Catal. Gen.* **2006**, *301*, 66–74. [CrossRef]
34. Galvita, V.V.; Semin, G.L.; Belyaev, V.D.; Yurieva, T.M.; Sobyanin, V.A. Production of Hydrogen from Dimethyl Ether. *Appl. Catal. Gen.* **2001**, *216*, 85–90. [CrossRef]
35. Busca, G. The Surface Acidity of Solid Oxides and Its Characterization by IR Spectroscopic Methods. An Attempt at Systematization. *Phys. Chem. Chem. Phys.* **1999**, *1*, 723–736. [CrossRef]
36. Can, F.; Courtois, X.; Duprez, D. Tungsten-Based Catalysts for Environmental Applications. *Catalysts* **2021**, *11*, 703. [CrossRef]
37. Macht, J.; Baertsch, C.D.; May-Lozano, M.; Soled, S.L.; Wang, Y.; Iglesia, E. Support Effects on Brønsted Acid Site Densities and Alcohol Dehydration Turnover Rates on Tungsten Oxide Domains. *J. Catal.* **2004**, *227*, 479–491. [CrossRef]
38. Hong, E.; Sim, H.-I.; Shin, C.-H. The Effect of Brønsted Acidity of WO_3 /ZrO_2 Catalysts in Dehydration Reactions of C3 and C4 Alcohols. *Chem. Eng. J.* **2016**, *292*, 156–162. [CrossRef]
39. Ladera, R.; Finocchio, E.; Rojas, S.; Busca, G.; Fierro, J.L.G.; Ojeda, M. Supported WO_x-Based Catalysts for Methanol Dehydration to Dimethyl Ether. *Fuel* **2013**, *113*, 1–9. [CrossRef]
40. Witoon, T.; Kidkhunthod, P.; Chareonpanich, M.; Limtrakul, J. Direct Synthesis of Dimethyl Ether from CO_2 and H_2 over Novel Bifunctional Catalysts Containing CuO-ZnO-ZrO_2 Catalyst Admixed with WO_x/ZrO_2 Catalysts. *Chem. Eng. J.* **2018**, *348*, 713–722. [CrossRef]
41. Suwannapichat, Y.; Numpilai, T.; Chanlek, N.; Faungnawakij, K.; Chareonpanich, M.; Limtrakul, J.; Witoon, T. Direct Synthesis of Dimethyl Ether from CO_2 Hydrogenation over Novel Hybrid Catalysts Containing a Cu ZnO ZrO_2 Catalyst Admixed with WO_x/Al_2O_3 Catalysts: Effects of Pore Size of Al_2O_3 Support and W Loading Content. *Energy Convers. Manag.* **2018**, *159*, 20–29. [CrossRef]
42. Pfriem, N.; Liu, Y.; Zahn, F.; Shi, H.; Haller, G.L.; Lercher, J.A. Impact of the Local Concentration of Hydronium Ions at Tungstate Surfaces for Acid-Catalyzed Alcohol Dehydration. *J. Am. Chem. Soc.* **2021**, *143*, 20133–20143. [CrossRef] [PubMed]
43. Baertsch, C.D.; Komala, K.T.; Chua, Y.-H.; Iglesia, E. Genesis of Brønsted Acid Sites during Dehydration of 2-Butanol on Tungsten Oxide Catalysts. *J. Catal.* **2002**, *205*, 44–57. [CrossRef]

44. Zhao, F.; Yi, L.; Deng, R.; You, K.; Song, J.; Jian, J.; Liu, P.; Ai, Q.; Luo, H. Supported WO_3/γ-Al_2O_3 as Bifunctional Catalyst for Liquid-Phase Highly Selective Oxidation of Cyclohexylamine to Cyclohexanone Oxime under Solvent-Free Conditions. *Mol. Catal.* **2019**, *475*, 110494. [CrossRef]
45. Said, A.E.-A.A.; Abd El-Wahab, M.M.M.; Abd El-Aal, M. Catalytic Dehydration of Methanol to Dimethyl Ether over Nanosized WO_3/Al_2O_3 System under Inert and Oxidative Atmosphere. *Mon. Chem. Chem. Mon.* **2016**, *147*, 1507–1516. [CrossRef]
46. Wachs, I.E. Raman and IR Studies of Surface Metal Oxide Species on Oxide Supports: Supported Metal Oxide Catalysts. *Catal. Today* **1996**, *27*, 437–455. [CrossRef]
47. Ross-Medgaarden, E.I.; Wachs, I.E. Structural Determination of Bulk and Surface Tungsten Oxides with UV−vis Diffuse Reflectance Spectroscopy and Raman Spectroscopy. *J. Phys. Chem. C* **2007**, *111*, 15089–15099. [CrossRef]
48. Chan, S. Laser Raman Characterization of Tungsten Oxide Supported on Alumina: Influence of Calcination Temperatures. *J. Catal.* **1985**, *92*, 1–10. [CrossRef]
49. Salvati, L.; Makovsky, L.E.; Stencel, J.M.; Brown, F.R.; Hercules, D.M. Surface Spectroscopic Study of Tungsten-Alumina Catalysts Using x-Ray Photoelectron, Ion Scattering, and Raman Spectroscopies. *J. Phys. Chem.* **1981**, *85*, 3700–3707. [CrossRef]
50. Martín, C.; Solana, G.; Malet, P.; Rives, V. Nb_2O_5-Supported WO_3: A Comparative Study with WO_3/Al_2O_3. *Catal. Today* **2003**, *78*, 365–376. [CrossRef]
51. Vermaire, D. The Preparation of WO_3/TiO_2 and WO_3/Al_2O_3 and Characterization by Temperature-Programmed Reduction. *J. Catal.* **1989**, *116*, 309–317. [CrossRef]
52. Grunert, W. Reduction Behavior and Metathesis Activity of WO_3/Al_2O_3 Catalysts I. An XPS Investigation of WO3/Al2O3 Catalysts. *J. Catal.* **1987**, *107*, 522–534. [CrossRef]
53. Rodríguez-Ramos, I.; Guerrero-Ruiz, A.; Homs, N.; de la Piscina, P.R.; Fierro, J.L.G. Reactions of Propene on Supported Molybdenum and Tungsten Oxides. *J. Mol. Catal. Chem.* **1995**, *95*, 147–154. [CrossRef]
54. Wang, H.; Wu, Y.; Liu, Z.; He, L.; Yao, Z.; Zhao, W. Deposition of WO_3 on Al_2O_3 via a Microwave Hydrothermal Method to Prepare Highly Dispersed W/Al_2O_3 Hydrodesulfurization Catalyst. *Fuel* **2014**, *136*, 185–193. [CrossRef]
55. Li, Y.; Wang, C.; Zheng, H.; Wan, F.; Yu, F.; Zhang, X.; Liu, Y. Surface Oxygen Vacancies on WO_3 Contributed to Enhanced Photothermo-Synergistic Effect. *Appl. Surf. Sci.* **2017**, *391*, 654–661. [CrossRef]
56. Soled, S. Comparison of the Acidities of WO_3/Al_2O_3 and Ultrastable Faujasite Catalysts. *J. Catal.* **1988**, *111*, 286–295. [CrossRef]
57. Chen, X.; Clet, G.; Thomas, K.; Houalla, M. Correlation between Structure, Acidity and Catalytic Performance of WO_x/Al_2O_3 Catalysts. *J. Catal.* **2010**, *273*, 236–244. [CrossRef]
58. Zhang, R.; Jagiello, J.; Hu, J.F.; Huang, Z.-Q.; Schwarz, J.A.; Datye, A. Effect of WO_3 Loading on the Surface Acidity of $WO_3/Al2O_3$ Composite Oxides. *Appl. Catal. Gen.* **1992**, *84*, 123–139. [CrossRef]
59. Rorrer, J.; He, Y.; Toste, F.D.; Bell, A.T. Mechanism and Kinetics of 1-Dodecanol Etherification over Tungstated Zirconia. *J. Catal.* **2017**, *354*, 13–23. [CrossRef]
60. Góra-Marek, K.; Tarach, K.; Choi, M. 2,6-Di- *Tert*- Butylpyridine Sorption Approach to Quantify the External Acidity in Hierarchical Zeolites. *J. Phys. Chem. C* **2014**, *118*, 12266–12274. [CrossRef]
61. Kitano, T.; Hayashi, T.; Uesaka, T.; Shishido, T.; Teramura, K.; Tanaka, T. Effect of High-Temperature Calcination on the Generation of Brønsted Acid Sites on WO_3/Al_2O_3. *ChemCatChem* **2014**, *6*, 2011–2020. [CrossRef]
62. Rossmedgaarden, E.; Knowles, W.; Kim, T.; Wong, M.; Zhou, W.; Kiely, C.; Wachs, I. New Insights into the Nature of the Acidic Catalytic Active Sites Present in ZrO_2-Supported Tungsten Oxide Catalysts. *J. Catal.* **2008**, *256*, 108–125. [CrossRef]
63. Fu, Y.; Hong, T.; Chen, J.; Auroux, A.; Shen, J. Surface Acidity and the Dehydration of Methanol to Dimethyl Ether. *Thermochim. Acta* **2005**, *434*, 22–26. [CrossRef]
64. Xu, M.; Lunsford, J.H.; Goodman, D.W.; Bhattacharyya, A. Synthesis of Dimethyl Ether (DME) from Methanol over Solid-Acid Catalysts. *Appl. Catal. Gen.* **1997**, *149*, 289–301. [CrossRef]
65. Sun, J.; Yang, G.; Yoneyama, Y.; Tsubaki, N. Catalysis Chemistry of Dimethyl Ether Synthesis. *ACS Catal.* **2014**, *4*, 3346–3356. [CrossRef]
66. Yaripour, F.; Baghaei, F.; Schmidt, I.; Perregaard, J. Catalytic Dehydration of Methanol to Dimethyl Ether (DME) over Solid-Acid Catalysts. *Catal. Commun.* **2005**, *6*, 147–152. [CrossRef]
67. Sabour, B.; Peyrovi, M.H.; Hamoule, T.; Rashidzadeh, M. Catalytic Dehydration of Methanol to Dimethyl Ether (DME) over Al-HMS Catalysts. *J. Ind. Eng. Chem.* **2014**, *20*, 222–227. [CrossRef]